

<https://doi.org/10.1038/s41612-024-00831-x>

Dry soil moisture on the Tibetan plateau drives synchronous extreme heatwaves in Europe and East Asia

Check for updates

Jilan Jiang¹, Yimin Liu^{2,3} ✉, Jun Meng⁴, Guoxiong Wu^{1,3}, Bian He^{2,3}, Tingting Ma⁵, Wen Bao⁶ & Jingfang Fan^{7,8} ✉

Recently, extreme heatwaves have frequently concurrently swept across Europe and East Asia, causing severe cascading socioeconomic consequences. However, the nonlinear synchronization relationship between these heatwaves and their underlying physical mechanisms remains poorly understood. Utilizing the event synchronization climate network method, atmospheric dynamic diagnostics, and numerical experiments, we revealed robust synchronization between heatwaves over Europe and East Asia, strongly associated with dry soil moisture conditions over the Tibetan Plateau from the preceding winter to summer. Dry soil moisture triggers an equivalent barotropic anticyclone north of the Tibetan Plateau, coinciding with the subtropical westerly jet waveguide and initiating circumglobal atmospheric Rossby waves propagating westward and eastward. Consequently, an equivalent barotropic anticyclone develops over Europe. These anticyclones induce simultaneous heatwaves across Europe and East Asia by increasing downward solar radiation and adiabatic sinking, amplified by positive land-atmosphere feedback. Our findings significantly enhance the understanding and predictive capabilities of these synchronous heatwaves across Eurasia.

Synchronous extreme heatwaves in the Northern Hemisphere have significantly increased since 1979 as global warming intensifies¹, with projections indicating a continued upward trend due to anthropogenic forcing^{2,3}. These synchronous heatwaves strike multiple regions simultaneously, exacerbate disasters, and substantially affect lives and socioeconomic development⁴. For example, the summer of 2022 exhibited concurrent extreme heatwaves over Europe and Southern China, causing heavy wildfires and energy shortages^{5–8}. The co-occurrence of European and East Asian heatwaves was also observed during the summer of 2010^{9,10}. Two pivotal questions emerge when considering the significant impact of synchronous extreme heatwaves on social well-being and environmental sustainability: To what extent do heatwaves occur simultaneously over Europe and East Asia, and what are the underlying physical mechanisms driving this synchronization?

To address the first question, our study utilized the event synchronization climate network method to uncover robust and significant synchronization in the occurrence of heatwaves between Europe and East Asia.

A climate network is a mathematical framework that represents the complex interactions between various components of a climate system^{11,12}. Specifically, the event synchronization climate network method^{11,13}, which defines synchronized events as occurrences that closely align within specified time intervals, has been used extensively to analyze synchronous extreme weather and climate events^{12,14–18}. For example, it has elucidated global synchronization patterns of extreme precipitation in South Asia¹². Previous studies have identified synchronous extreme heatwaves over South Europe and Northeast Asia, as well as over East Europe and North China, using Empirical Orthogonal Function analysis^{19,20}. Our study revealed a strong synchronization between Europe and central East Asia. This finding highlighted the advantage of employing the event synchronization climate network method, revealing previously unknown extreme heatwave synchronous patterns between Europe and central East Asia.

To address the second question, our study investigated the linkage between synchronous extreme heatwaves over Europe and East Asia and dry soil moisture conditions over the Tibetan Plateau (TP), elucidating the

¹State Key Laboratory of Numerical Modeling for Atmospheric Sciences and Geophysical Fluid Dynamics, Institute of Atmospheric Physics, Chinese Academy of Sciences, Beijing, China. ²Key Laboratory of Earth System Numerical Modeling and Application, Institute of Atmospheric Physics, Chinese Academy of Sciences, Beijing, China. ³University of Chinese Academy of Sciences, Beijing, China. ⁴School of Science, Beijing University of Posts and Telecommunications, Beijing, China. ⁵China Meteorological Administration Training Centre, Beijing, China. ⁶Chinese Research Academy of Environmental Sciences, Beijing, China. ⁷School of Systems Science, Beijing Normal University, Beijing, China. ⁸Potsdam Institute for Climate Impact Research, Potsdam, Germany.

✉ e-mail: lym@lasg.iap.ac.cn; jingfang@bnu.edu.cn

associated physical mechanisms through atmospheric dynamics diagnostics and numerical experiments. Previous studies predominantly identified the role of high-amplitude waves resulting from planetary wave resonance^{21–24} and large-scale atmospheric teleconnection⁵ as contributors to synchronous events in the Northern Hemisphere. However, what causes the anomalous planetary waves or teleconnections and studies on the role of the TP are relatively limited. The TP’s unique geographical characteristics are crucial in the weather and climate patterns across East Asia and globally^{25–28}. Its impact extends widely, influencing extreme precipitation and drought in East China^{29,30} and shaping the temperature and precipitation in West Asia, North Africa, and South Europe via Rossby wave trains and zonal overturning atmospheric circulation^{31–33}. Importantly, the influence of the TP extends upstream and downstream³⁴, affecting extreme heatwaves over South Europe and Northeast Asia¹⁹. The summer snow cover over the western TP notably impacts the variability of concurrent compound heatwaves in the Northern Hemisphere³⁵. We emphasized that dry soil moisture conditions over the TP lead to simultaneous extreme heatwaves over Europe and East Asia by initiating circumglobal Rossby waves; this synchronization pattern is facilitated by a positive land-atmosphere feedback loop involving atmospheric circulation, soil moisture, and temperature over the heatwave regions.

Our study highlighted the critical issue of synchronous extreme heatwaves between Europe and East Asia in the context of global warming. By utilizing advanced methodologies such as the event synchronization climate network method, atmospheric dynamic diagnostics, and numerical simulation, we revealed a robust synchronization of these events, driven by dry soil moisture conditions over the TP. Our findings also underscored the complex interplay among atmospheric dynamics, soil moisture, and temperature, providing crucial insights for predicting and mitigating the impacts of simultaneous extreme heatwaves in a warming world.

Results

Synchronous features of Eurasian extreme heatwaves

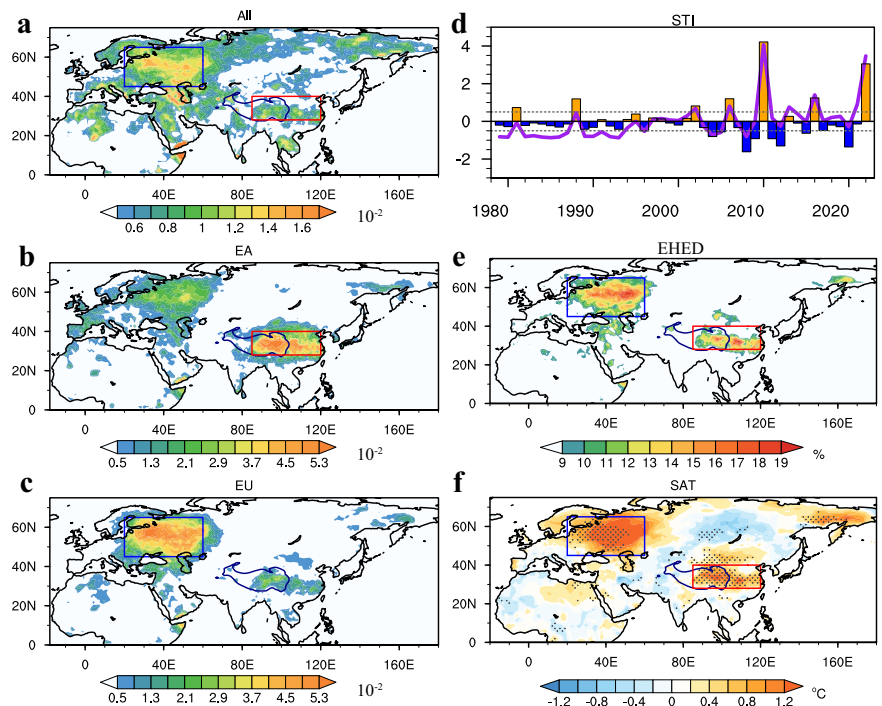
Conventionally, heatwave events are treated as single occurrences in event synchronization calculations¹⁸. However, this methodology overlooks event duration, with extreme event indices often infrequent, potentially compromising synchronization accuracy owing to insufficient data points. In

this study, we introduced the “*Index of Extreme Heatwave Event Days (IEHED)*” assigning a value of one to days within heatwave periods and zero otherwise. This index quantifies the heatwave occurrence and duration in the study region. The synchronization of heatwaves between regions was defined by the calculated number of days with simultaneous heatwaves, represented as the scalar product of the heatwave indices for both regions (for detailed methodology, please refer to the Methods section). In other words, it involves multiplying the corresponding values of the heatwave indices for the same days in both regions and summing these products to obtain a measure of how closely the heatwave occurrences align across these regions. A higher scalar product indicates a stronger synchronization of heatwaves between regions.

In this study, we constructed a series of climate networks using the *IEHED* spanning from June 1 to August 31 of each calendar year for each node in the Northern Hemisphere with a spatial resolution of $1^\circ \times 1^\circ$. Nodes are connected if their scalar products exceed 95% of the non-zero synchronization values of all pairs of nodes. A shuffle test scheme was also used as a comparative analysis to determine the significance of synchronization, which shows consistent results (see more in the Methods section).

The degree of each node is computed as the ratio of its connected links relative to the total links, with higher node degrees indicating more connections to other regions. Notably, the regions concentrated in Europe, key areas of East Asia, North Africa, the Arabian Peninsula, the Indochina Peninsula, and Eastern Siberia exhibit relatively high degrees (Figs. 1a, S1a, 2a, d). This suggests that these areas tend to experience synchronized heatwaves with other Eurasian regions. Specifically, in the synchronous network based on the synchronization relationship between nodes over the entire Eurasian and key East Asian regions, high degrees are observed over the local and European region, denoting that East Asia has a strong remote connection with Europe (Figs. 1b, S1b, 2b, e). Conversely, when the network is constructed based on the European region, high degrees are observed over the local and key East Asian region (Figs. 1c, S1c, 2c, f). These findings underscore the strong synchronization of heatwaves between these two regions. The synchronous pathways of extreme heatwaves over the key regions of Europe and East Asia also perfectly illustrate their interconnections (Fig. 2). Furthermore, the probability distribution of the significant links between the key European and East Asian regions across various

Fig. 1 | Synchronization relationship between European and East Asian summertime extreme heatwaves. a–c Degree of synchronization network nodes derived based on grid points over the entire Northern Hemisphere Eurasia-African (a), key East Asian (b), and key European (c) regions. d Normalized raw synchronization teleconnection index (purple line) and its interannual component (bar); Gray dashed lines indicate the ± 0.5 standard deviation. Percentage (units: %) of total summertime extreme heatwave event days (EHEDs) relative to the total days (e) and the composite of June–July–August-averaged daily surface maximum air temperature anomalies (f; units: $^\circ\text{C}$) during the seven strong synchronization years. Dots in (f) indicate significance at the 0.05 significance level. Blue and red boxes indicate the key European ($45^\circ\text{--}65^\circ\text{N}$, $20^\circ\text{--}60^\circ\text{E}$) and East Asian ($28^\circ\text{--}40^\circ\text{N}$, $85^\circ\text{--}120^\circ\text{E}$) regions, respectively. Dark blue contours show the 3000 m topographic height. Dataset derived from CPC.



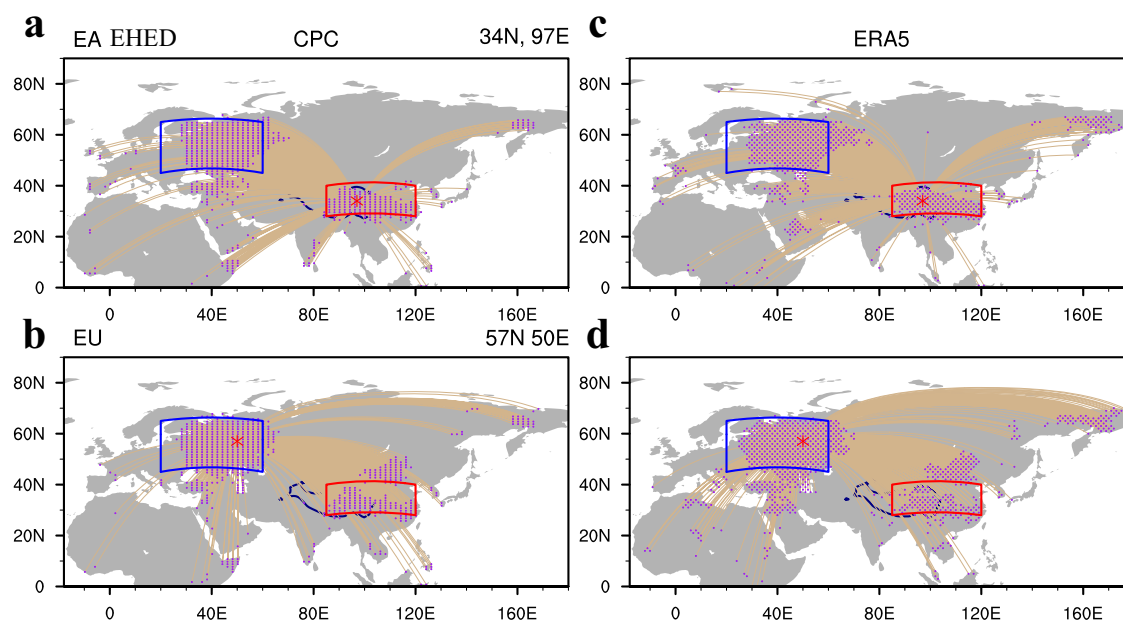


Fig. 2 | Synchronous pathway of European and East Asian summertime extreme heatwaves. Synchronous pathways based on the EHEDs at 34°N, 97°E (*; **a, c**) and 57°N, 50°E (*; **b, d**) points for CPC (**a, b**) and ERA5 (**c, d**) datasets. Purple dots

represent the endpoints of synchronous pathways. Pathways are shown with one grid interval. Blue and red boxes indicate the key European and East Asian regions, respectively. Dark blue contours show the 3000 m topographic height.

distances reveals two prominent peaks. The highest probability occurs within a few hundred kilometers, indicating strong local synchronization, whereas a secondary peak appears beyond 3000 km, suggesting long-range synchronization (not shown). This pattern is consistent with previous studies on the synchronization features of extreme rainfall events^{12,17}.

Moreover, to investigate the dynamic evolution of the synchronization relationship between extreme heatwaves over Europe and East Asia, we introduced a *synchronization teleconnection index*¹⁷, defined as the sum of links with non-zero synchronization values in the network constructed based on the synchronization relationship between heatwaves over two key regions (Methods). This index exhibits larger interannual variability after the year 2000 than before (Figs. 1d and S1d), with a significant difference (1.69) in the inter-annual variance between the period of 2000–2022 (1.85) and 1979–1999 (0.16), at the 0.01 level based on the F-test (Fig. 1d). This indicates a notable increase in the variability of synchronous extreme heatwaves between Europe and East Asia.

To confirm the effectiveness of the synchronization teleconnection index in representing the synchronization of the European-East Asian heatwaves, we examined the seven strongest synchronization years based on this index. These years are 1981, 1988, 2002, 2006, 2010, 2016, and 2022 for CPC dataset, and the ERA5 dataset presents the results, except for one additional year, 1998 (Figs. 1d and S1d). The percentile of total extreme heatwave event days relative to the total days for these years, as well as the composite of the corresponding summer mean daily surface maximum air temperature anomalies, indeed show concurrent large values in key regions of Europe and East Asia, suggesting that the two areas experience numerous synchronized extreme heatwaves during these years (Figs. 1e, f, S1e, f). These observations highlight the real synchronous pattern of extreme heatwaves and the effectiveness of this synchronization teleconnection index in representing synchronization relationships.

Relationship between Eurasian synchronous extreme heatwaves and the TP soil moisture

What causes the synchronous extreme heatwaves over key European and East Asian regions? We investigated various forcing factors and found that dry TP soil moisture conditions, especially in the western TP, persist from the preceding winter to summer and play a vital role in the occurrence of

strong synchronous extreme heatwaves (Figs. 3a–c, S3). Previous studies have indicated that soil moisture can have local and remote impacts by exciting anomalous large-scale circulation patterns^{36–38}. Meanwhile, land surface factors over the TP are critically important in land-atmosphere energy and water exchange process^{26,39}. Thus, it is meaningful to investigate the role of TP soil moisture.

The synchronization teleconnection index exhibits a significant negative correlation with the TP soil moisture index, defined as area-averaged 1–4-layer soil moisture anomalies in the region of 31°–35°N, 80°–103°E, from the preceding winter to summer, with the highest correlation coefficient reaching approximately -0.65 in summer ($p < 0.01$; Table 1). A stable negative correlation is observed from 1995 onwards (Fig. 3h). When the interannual TP soil moisture index is less than -1 standard deviation, it is defined as a dry soil moisture year. The seven strongest dry years are identified as 1995, 2002, 2006, 2010, 2015, 2016, and 2022. Notably, 71% of these dry soil moisture years (excluding 1995 and 2015) coincide with strong synchronous extreme heatwaves (Fig. 3g).

The above results indicate an interannual connection between Eurasian synchronous extreme heatwaves and soil moisture over the TP. While heatwaves typically occur on daily to subseasonal time scales, seasonal soil moisture anomalies provide only background conditions for these events. To further investigate their nonlinear relationship from a daily time scale, we constructed a series of synchronous networks linking extreme heatwave event days across the entire Northern Hemisphere Eurasia-African continent and extremely dry soil moisture days over the key TP region (Methods). Prominent centers of node degree are observed over Europe and East Asia, with higher values indicating a closer relationship between extreme heatwaves and dry soil moisture (Fig. 3d). Interestingly, when extremely dry soil moisture days lead by 10 or 20 days ahead of extreme heatwaves, centers of high values still appear over Europe and East Asia (Fig. 3e, f). This suggests that dry soil moisture conditions over the TP could develop prior to the occurrence of extreme heatwaves in Europe and East Asia. These findings provide additional evidence of the potential role of TP soil moisture in triggering synchronous extreme heatwaves. The consistency of results based on different lead times also suggests the persistence of soil moisture. Overall, both seasonal background conditions and daily-subseasonal variability are favorable for the synchronous occurrence of heatwaves over Eurasian regions.

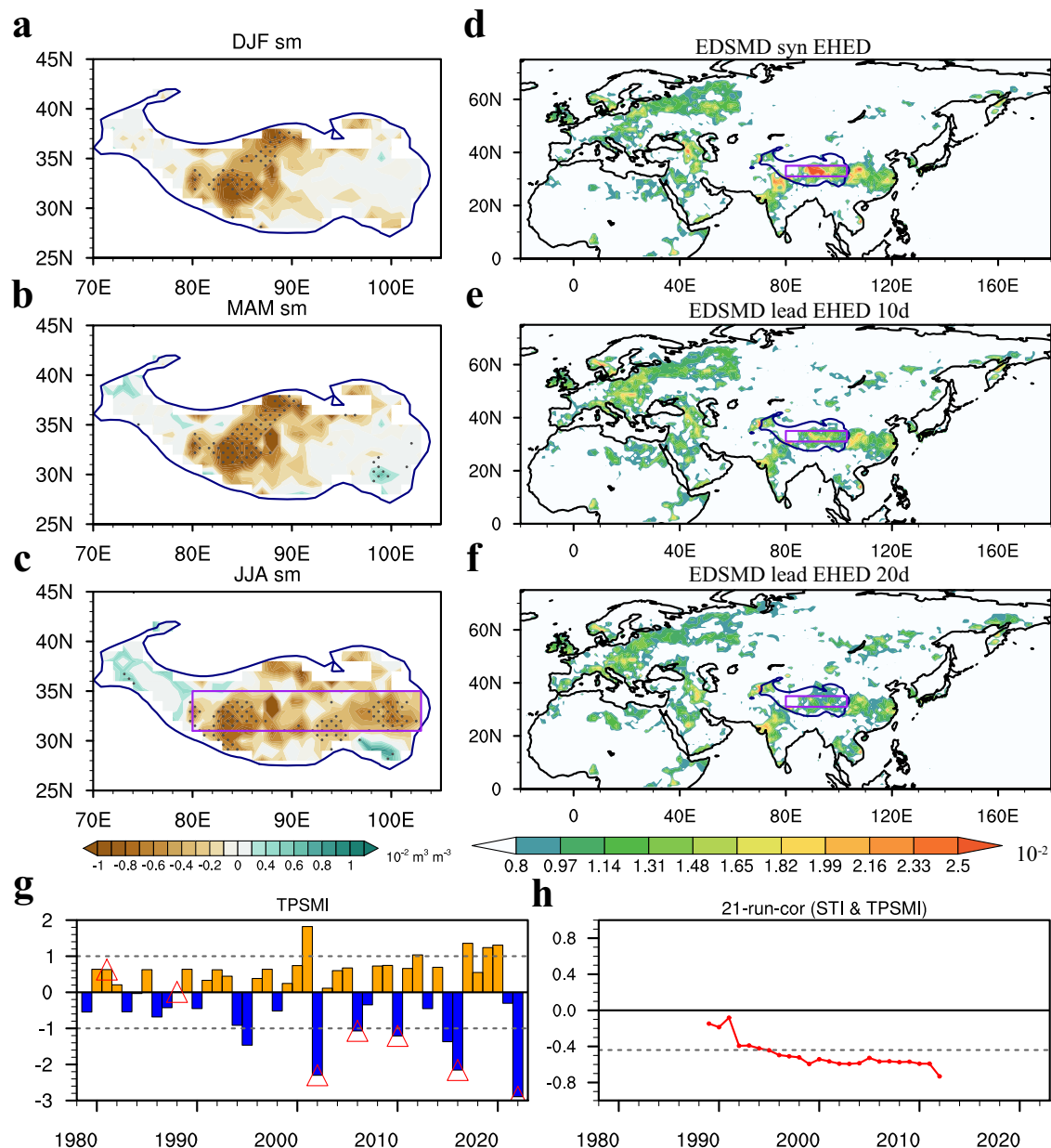


Fig. 3 | Relationship between European and East Asian summertime synchronous extreme heatwaves and soil moisture over the Tibetan Plateau (TP). Composite of December–January–February (a), March–April–May (b), and June–July–August (c)–averaged soil moisture anomalies (unit: $10^{-2} \text{ m}^3 \text{ m}^{-3}$) for the ERA5 dataset based on the seven strong synchronization years; **d** Degree of network nodes based on the synchronization of EHEDs over the Northern Hemisphere Eurasia–African region and extreme dry soil moisture days (EDSMDs; Methods) in the key TP region (purple box); Degree of network nodes with EDSMDs

leading by 10 (e) and 20 (f) days ahead of EHEDs. **g** Normalized interannual component of TP soil moisture index; Gray dashed lines indicate the ± 1 standard deviation; Red triangles mark seven strong synchronization years. **h** The 21-year sliding correlation coefficient between the TP soil moisture index and synchronization teleconnection index; The gray dashed line denotes 0.05 significance level. Purple boxes in (c)–(f) indicate the key region ($31^{\circ} - 35^{\circ}\text{N}$, $80^{\circ} - 103^{\circ}\text{E}$) used to define the TP soil moisture index. Dark blue contours show the 3000 m topographic height.

Physical mechanisms of dry TP soil moisture triggering Eurasian synchronous extreme heatwaves

The following section examines the physical processes through which the dry TP soil moisture triggers favorable atmospheric circulation conditions for synchronous extreme heatwaves across Eurasia. Dry soil moisture over the TP amplifies the upward sensible heat flux and subsequently warms the atmosphere. The primary heating center is situated in the central TP (Figs. 3a–c, S4f). Interestingly, because of the horizontal inhomogeneous heating⁴⁰, a significant maximum response in the geopotential height and wind fields emerges at a higher latitude north of the heating center during summer, that is, an equivalent barotropic anticyclone develops north of the TP (Figs. 4a, S4a–c).

These strong upper-tropospheric anticyclonic disturbances coincide with the Eurasian westerly wind-jet waveguide, facilitating the eastward propagation of disturbances^{41,42}. Subsequently, a Rossby wave train is initiated and propagates across the entire Northern Hemisphere (Figs. 4a and S4a). Previous studies have demonstrated the influence of the TP on the upstream circulation through the westward propagation of Rossby waves³². In our study, results from the Linear Baroclinic Model experiment, which was forced by the prescribed positive diabatic heating over the TP (details in the Method section), verify the westward Rossby wave response and eastward-propagating wave train along the westerly jet (Figs. 4b, c, S5), which is consistent with previous findings^{34,43}. Initially, the 200-hPa geopotential height response occurs around the heating region, and then zonally

Table 1 | Pearson linear correlation between the synchronization teleconnection index (STI) and Tibetan Plateau soil moisture index (TPSMI)

Correlation coefficient	DJF TPSMI	MAM TPSMI	JJA TPSMI
CPC STI	-0.36**	-0.38**	-0.64***
ERA5 STI	-0.40***	-0.45**	-0.65***

DJF, MAM, and JJA TPSMI represent the December–January–February, March–April–May, and June–July–August-averaged TPSMI derived from ERA5 dataset, respectively. *, **, and *** indicate significance at 0.1, 0.05, and 0.01 levels, respectively.

propagates westward in subsequent days. This wave reaches the key European region by approximately day 10 and stabilizes around day 15. The westward propagation of Rossby waves presents the upstream development of anomaly of the same sign as the original⁴⁴. In other words, it is the propagation of phase without the generation of new disturbances upstream of the initial disturbance (Fig. S5c–f). While the eastward propagation of stationary waves on a zonally varying basic flow is the propagation of Rossby wave packets or wave energy. They can facilitate the development of new disturbances downstream with the role of the westerly jet waveguide^{41,44–46}. Additionally, it also can be noted that the local anticyclone center is positioned north of the TP as the response stabilizes (Fig. 4b, c).

Consequently, significant equivalent barotropic anticyclonic circulations are established over Europe, together with anticyclonic circulations over the northern TP, collectively contributing to the European–East Asian synchronous extreme heatwave pattern (Figs. 1e, f, S1e, f, 4a–c). The development of high-pressure systems decreases medium-low cloud cover, allowing more solar shortwave radiation to reach and warm the surface (Fig. S4d, e). The warm surface further heats the air through the upward surface longwave radiation flux and sensible heat flux (Fig. S4f). Additionally, anomalous easterly winds on the southern side of the upper tropospheric anticyclonic circulation north of the TP also reduce the westerly jet over the TP and its eastern regions, facilitating the development of upper-level convergence and adiabatic subsidence, further warming the atmosphere^{47,48} (Figs. 4a, S5a). These anomalies are consistent with the composite results of the strong synchronous extreme heatwave cases (not shown).

We also performed soil moisture sensitivity numerical experiments using the Community Atmosphere Model version 6 (CAM6, Methods) to understand and confirm the role of reduced TP soil moisture in the occurrence of European–East Asian synchronous extreme heatwaves (Figs. 4d, e, S6a). Differences between experiments forced by the global climatological monthly mean soil moisture and the corresponding soil moisture over the TP multiplied by 0.5 demonstrate the climate effects of dry soil moisture conditions over the TP. Our results show the emergence of an anticyclonic circulation north of the TP and the propagation of a circumglobal stationary Rossby wave train, subsequently establishing an anticyclonic circulation over Europe (Fig. 4d). A slight eastward and northward shift is noted when the simulated wave train was compared with the observations. This is attributed to the northward shift of the simulated Eurasian subtropical jet (Fig. 4a, d). Generally, key European and East Asian regions are controlled by positive geopotential height anomalies, which contribute to the development of positive surface air temperature anomalies (Fig. 4d, e). Significant negative temperature anomalies are also observed over the Indian Subcontinent, consistent with the findings of Ref. 27, who examined the temperature response to sensible heating over the TP. Simultaneously, the establishment of high-pressure systems inhibits precipitation, leading to dry soil moisture in the heatwave regions (Fig. S6b). In turn, the dry soil moisture intensifies the positive height anomalies at the upper levels, making them more persistent. This indicates the existence of a positive land-atmosphere feedback mechanism involving atmospheric circulation, soil moisture, and temperature, which is extremely important for the formation and maintenance of extreme heatwaves^{7,49}.

Discussion

Recently, the number of synchronous extreme heatwave events across the Northern Hemisphere has increased, often resulting in cascading disasters^{1,23}. Precisely quantifying synchronous extreme heatwaves and investigating their formation mechanisms are vital for addressing climate change challenges and fortifying disaster prevention measures. Conventional climatological statistical methods frequently struggle with the complex nonlinear relationships between extreme heatwaves in disparate regions. As presented in Table S1, the Pearson linear correlation coefficients between the number of extreme heatwave events in key regions of Europe and East Asia, as well as extreme heatwave event days, reveal an insignificant relationship between extreme heatwaves in these two regions, with only a weak positive correlation observed for summer mean surface air temperature. In contrast, the event synchronization climate network method effectively captures the synchronization relationship between extreme heatwaves in Europe and East Asia. This underscores the non-negligible nonlinearity of the synchronization relationship between extreme heatwaves in these regions, and the climate network method has potential advantages for addressing this nonlinear synchronicity. Furthermore, by combining atmospheric dynamic diagnostics and numerical experiments, our study highlights the crucial role of dry TP soil moisture conditions in the development of synchronous extreme heatwaves. Our findings also hold promise for improving the prediction of extreme events. By identifying precursor factors such as TP soil moisture anomalies, our study lays the groundwork for enhancing predictive models. Integrating these findings into existing prediction frameworks could lead to more accurate forecasts, helping to mitigate the impacts of extreme heatwaves through better preparedness and response strategies.

However, it is important to acknowledge several limitations and uncertainties inherent in our approach. The event synchronization climate network method, while effective in capturing nonlinear relationships, relies on certain assumptions about event timing and thresholds that may influence the results. The spatial and temporal resolution of the datasets used, particularly in capturing soil moisture dynamics over the TP, may introduce uncertainties in our findings. Additionally, the complex interactions between land surface processes and atmospheric circulation are not fully captured in our study, and there may be other contributing factors or feedback mechanisms that remain unexplored. Future studies should consider these limitations and aim to refine the methodologies and datasets to reduce these uncertainties.

Moreover, our study focuses primarily on the synchronization relationship between extreme heatwaves at a regional scale, specifically between Europe and East Asia. Expanding this research to a hemispheric or even global scale could uncover additional synchronization patterns, offering a more comprehensive understanding of these phenomena across different regions. This broader perspective is crucial for capturing the full complexity of climate synchronization and for understanding how regional interactions contribute to global climate dynamics.

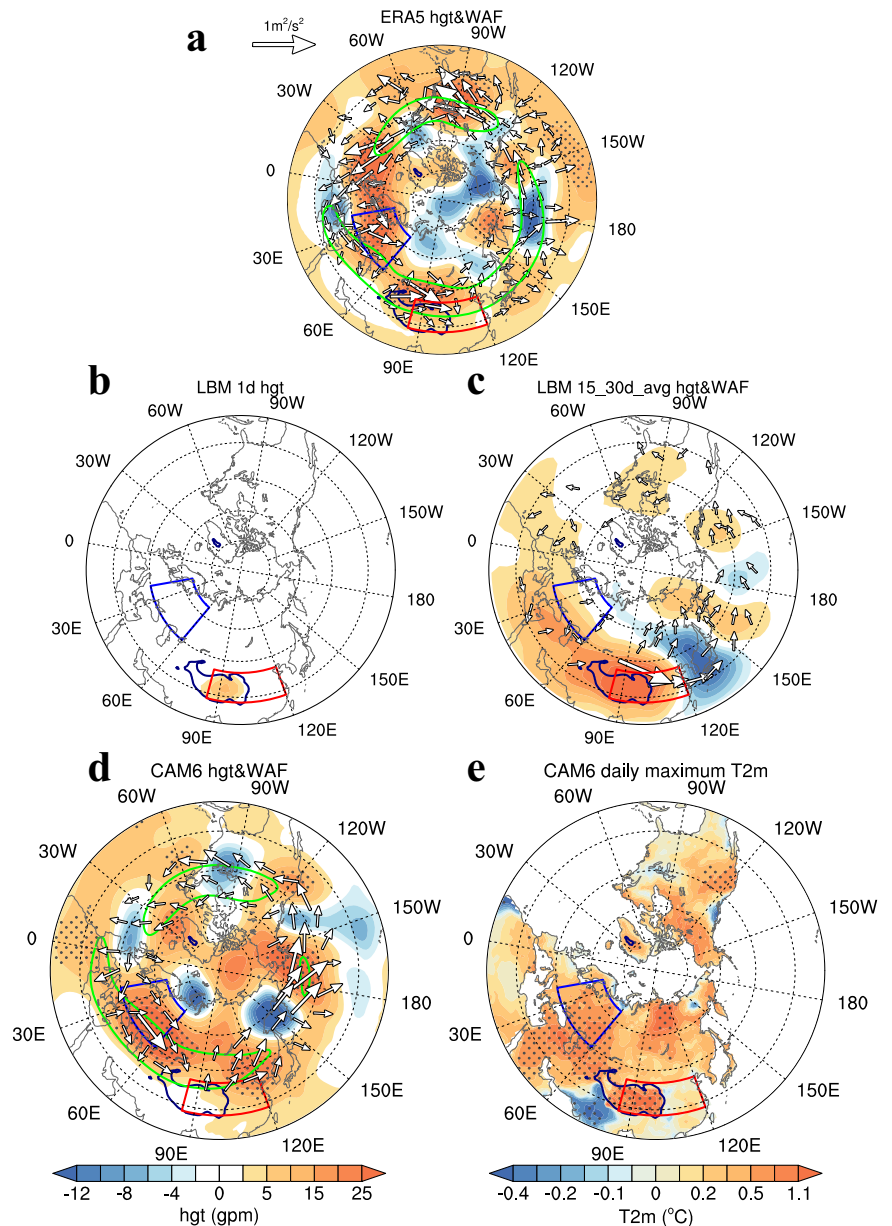
Overall, the framework proposed in this study, which integrates complex system dynamics with atmospheric dynamics, offers a novel approach for quantifying the nonlinear synchronicity of extreme weather and climate events. This approach not only enhances our understanding of the underlying physical mechanisms but also underscores the need to explore its application in other regions and at different spatial and temporal scales. By doing so, we can further unravel the sophisticated physical processes driving extreme events and develop more effective strategies for climate risk management and adaptation.

Methods

Observation and reanalysis of data

The datasets used in this study include the following: (1) daily surface maximum temperature and monthly surface soil moisture (mm) obtained from the Climate Prediction Center (CPC) of the National Oceanic and Atmospheric Administration (NOAA) span from 1979 to 2022 and have a spatial resolution $0.5^\circ \times 0.5^\circ$ ⁵⁰. We reshaped the resolution to $1^\circ \times 1^\circ$ by

Fig. 4 | 200-hPa circulation and surface air temperature anomalies associated with dry TP soil moisture conditions. **a** 200-hPa geopotential height anomalies (shading, unit: gpm) and wave activity flux (vectors, unit: $\text{m}^2 \text{s}^{-2}$) for June–July–August-averaged composite results based on seven strong dry TP soil moisture years from the ERA5 dataset; **b** 200-hPa geopotential height (shading, unit: gpm) response on day 1 (**b**) and 200-hPa geopotential height (shading, unit: gpm) and wave activity flux (vectors, unit: $\text{m}^2 \text{s}^{-2}$) response averaged over days 15–30 (**c**) to the prescribed heating of key TP region in the linear baroclinic model; **d** June–July–August-averaged 200-hPa geopotential height (shading, unit: gpm) and wave activity flux (vectors, unit: $\text{m}^2 \text{s}^{-2}$) response to the dry TP soil moisture condition in the CAM6; **e** June–July–August-averaged daily maximum 2 m air temperature (shading, unit: $^{\circ}\text{C}$) response in the CAM6; The green contour indicates the climatological 20 m s^{-1} zonal wind at 200-hPa for ERA5 dataset (**a**) and the CAM6 result (**d**), indicating the location of the westerly jet. Dots in (**a**), (**d**), and (**e**) indicate the significance at the 0.05 significance level. Blue and red boxes indicate the key European and East Asian region, respectively. Dark blue contours show the 3000 m topographic height.



using grid points with an interval to save computation. (2) The monthly soil moisture data (kg m^{-2} ; 2000 to 2022) sourced from the Global Land Data Assimilation System (GLDAS) Noah Land Surface Model L4 Version 2.1 were available from 2000 to 2022⁵¹. These data are at 0–10, 10–40, 40–100, and 100–200 cm depths and have a spatial resolution of $1^{\circ} \times 1^{\circ}$. (3) The monthly soil moisture data ($\text{m}^3 \text{m}^{-3}$) at 0–10, 10–40, 40–100, and 100–200 cm depths were calculated from daily data from 1998 to 2020 derived from the China Meteorological Administration Land Data Assimilation System (CLDAS)⁵². This dataset is at a horizontal resolution of $0.0625^{\circ} \times 0.0625^{\circ}$, covering 0° – 65°N , 60° – 160°E region. (4) The monthly three-dimensional atmospheric circulation at 37 pressure levels, mean surface heat flux, and cloud cover were provided by the fifth-generation atmospheric reanalysis (ERA5) produced by the European Center for Medium-Range Weather Forecasts⁵³. Monthly and daily maximum 2 m air temperature and soil moisture ($\text{m}^3 \text{m}^{-3}$) at depths of 0–7, 7–28, 28–100, and 100–289 cm was derived from ERA5-land reanalysis⁵⁴. These datasets are at a horizontal resolution of $1^{\circ} \times 1^{\circ}$, covering the period of 1979–2022.

Definition of extreme heatwave event days and extreme dry soil moisture days

An extreme heatwave day was identified when the temperature on the target day exceeded the 90th percentile threshold. This threshold was defined as the 90th percentile of daily temperatures for a total of 660 days (44 years \times 15 days, including 7 days before and after the target day) in the 44 years from 1979 to 2022. When an extreme heatwave condition persisted for 3 days or more, it was defined as an extreme heatwave event, with each day within this event referred to as an extreme heatwave event day¹⁸. Only the heatwaves in June, July, and August from 1979 to 2022 were analyzed in this study. Considering the sensitivity of extreme events to threshold selection, we employed the 95th percentile threshold for the comparative analysis.

An extremely dry soil moisture day was identified when the soil moisture on the target day was less than the 10th percentile threshold. This threshold was defined as the 10th percentile of daily soil moisture for a total of 660 days (44 years \times 15 days; including 7 days before and after the target day) in the 44 years from 1979 to 2022 for the ERA5 dataset.

Event synchronization climate network method

Previous studies^{12,17,18} have evaluated the synchronization of extreme rainfall and heatwave events based solely on event series, neglecting differences in event duration. However, for heatwaves, the duration of the disparate events varies considerably. For example, the longest extreme heatwave event in the Northern Hemisphere Eurasia-African region lasted for 74 days at 10.75°N, 47.25°E grid point for the period 1979–2022, whereas the shortest event only persisted 3 days. In this study, we established the synchronization relationship of extreme heatwaves based on the sum of the scalar product of the “Index of Extreme Heatwave Event Days (IEHED)” between different regions. The specific calculation steps are as follows.

First, we defined an IEHED, where every extreme heatwave event day is assigned a value of “1”, and days with no heatwave occurrence are designated as “0”. e_i^y and e_j^y represent the index series for the y th year at grid points i and j , respectively. The heatwave synchronization of the y th year between grids i and j was defined as the sum ($ES_{i,j}^y$) of the scalar products of e_i^y and e_j^y , as expressed in Eq. (1):

$$ES_{i,j}^y = \sum_{i,j} e_i^y \cdot e_j^y \tag{1}$$

Subsequently, a climate network was constructed by treating each grid as a node and characterizing the links between the nodes through heatwave synchronization. We considered two nodes to be significantly connected if their synchronization value was within the strongest 5% of all node pairs across all years¹⁸. If θ represents the 95th quantile of all non-zero synchronization values, the adjacency matrix of the network was defined as follows:

$$A_{i,j}^y = \begin{cases} 1, & \text{if } ES_{i,j}^y > \theta; \\ 0, & \text{else} \end{cases} \tag{2}$$

To increase the credibility of the results, the statistical significance of the links between nodes was also estimated by the shuffle test scheme. We conducted shuffle processing for the time series of the original data and then calculated the heatwave synchronization between node pairs after shuffle processing¹⁷. This shuffle process was repeated 100 times, and the 95th percentile of its distribution was considered as the significance threshold θ for every node. Considering the consistency of the results (Figs. 1b, c, S7), the significance of the synchronization shown in this study was tested using a threshold test scheme, except for Figure S7, which was tested using a shuffle test scheme.

The degree P_j , quantifying the strength of the heatwave synchronization between node j and the other nodes, was defined as the ratio of significantly connected links relative to the total links:

$$P_j = \frac{\sum_{y=1}^Y \sum_{i=1}^N A_{i,j}^y}{Y \times N} \tag{3}$$

where Y and N represent the total number of years and grids in the key region, respectively. A larger P_j value indicates that grid j has a more significant connection with other grids. An Event Synchronization Method with varying temporal delays within a maximum of 10 days^{12,17} was employed for comparative analysis, in which the result presents less significance than that obtained by using extreme heatwave event days (Figs. 2 and S8).

In Eq. (3), if i and j both represent the grid points across the entire Eurasian land region, totaling $N = 9199$ grid points, then P_j denotes the synchronization of grid j with other grids in the Eurasian area (Figs. 1a, S1a, 2a, d). When i represents grid points in the key East Asian land region, with $N = 419$ grid points, P_j indicates the synchronization of grid j with all grids in East Asia (Figs. 1b, S1b, 2b, e). Conversely, for the key European land region, which comprises $N = 784$ grid points, the same principle applies (Figs. 1c, S1c, 2c, f).

Following Refs.12, 17, the probability of significant synchronization links for a specific grid point at a given distance r was computed as:

$$P(r) = \frac{X_0}{X_1} \tag{4}$$

where X_1 is the total number of edges within the distance range $r_0 \leq r \leq r_0 + l$, and X_0 denotes the number of significant links within this range. l represents the separation interval distance. If $P(r) = 0$, then there are no significant links at distance r for the grid point. Conversely, if $P(r) = 1$, all the links are significant, indicating strong synchronization. Finally, the average probabilities in the key European and East Asian regions are shown.

For a more intuitive representation of the synchronization of extreme heatwaves between Europe and East Asia, a synchronization teleconnection index (STI) was constructed as follows¹⁷:

$$STI^y = \sum_{i=1}^N \sum_{j=1}^M A_{i,j}^y; A_{i,j}^y = \begin{cases} 1, & \text{if } ES_{i,j}^y > 0; \\ 0, & \text{else} \end{cases} \tag{5}$$

where N and M represent the total numbers of grids in the key regions of Europe and East Asia, respectively, and y denotes the year. A higher STI indicates a greater level of synchronization in extreme heatwaves occurring over Europe and East Asia. When the STI exceeds 0.5 standard deviation, a strong synchronization year is defined.

Additionally, based on the synchronization between the extreme heatwave event days over the Northern Hemisphere Eurasia-African region and extreme dry soil moisture days in the key Tibetan Plateau (TP) region, we constructed climate networks illustrating the close connection between Eurasian synchronous extreme heatwaves and dry soil moisture conditions over the TP. When accounting for the lead-lag time, a climate network that reflects the lead-lag relationship between extreme heatwaves and extremely dry soil moisture was constructed. The calculation process is outlined above. That is, if e_j^y represent the extreme heatwave index series for the y th year at grid point j over the Northern Hemisphere Eurasia-African land region, and e_i^y represent dry soil moisture index series at grid points i over the key TP regions, then P_j indicates the synchronization between heatwaves at grid point j and soil moisture in TP regions.

Wave activity flux

The horizontal wave activity flux, which can illustrate the propagation of stationary Rossby waves, was calculated using the following formula⁴⁶:

$$W = \frac{P}{2|\vec{V}|} \left\{ \begin{aligned} & \overline{u}(\varphi_x'^2 - \varphi' \varphi_{xx}') + \overline{v}(\varphi_x' \varphi_y' - \varphi' \varphi_{xy}') \\ & \overline{u}(\varphi_x' \varphi_y' - \varphi' \varphi_{xy}') + \overline{v}(\varphi_y'^2 - \varphi' \varphi_{yy}') \end{aligned} \right. \tag{6}$$

In this equation, the overbars and primes indicate the mean flows and anomalies, respectively, relative to the climatology. P , $\vec{V} = (u, v)$, and φ denote the pressure, horizontal wind velocity, and geostrophic stream functions, respectively. Subscripts x and y represent the zonal and meridional derivatives, respectively. A zonally varying basic flow is employed in this method.

Other statistical methods

In this study, we also used composite analysis and linear correlation. Bootstrap resampling^{55,56} was employed to assess the statistical significance of composite results. The significance of the correlation coefficients was determined using a two-tailed Student’s t -test. The interannual variability of variables was obtained using a 2–9 years bandpass Lanczos filter after removing the linear trend. Unless otherwise stated, the boreal summer was defined as June, July, and August.

Models and numerical experiment designs

We employed a linear baroclinic model (LBM)²⁷ to investigate the daily atmospheric circulation response to prescribed diabatic heating over the TP. The fundamental principle of this model is to solve the primitive equations while considering the given basic state and thermal force. Atmospheric circulation variables and temperature data derived from the NCEP-NCAR reanalysis were employed as model inputs, and a time integration scheme was implemented to derive a stable response. The model features a vertical resolution of 20 levels and a horizontal resolution of T42. The model was integrated for 30 days and reached a steady state after approximately 15 days⁵⁸.

Additionally, the atmospheric and land components of the Community Earth System Model (version 2.1.3), namely the Community Atmosphere Model version 6 (CAM6) and the Community Land Model version 5 (CLM5), respectively, were used to validate and understand the physical mechanisms associated with dry soil moisture over the TP affecting the European-East Asian synchronous extreme heatwaves⁵⁹. The CAM6 operates at a horizontal resolution of $0.9^\circ \times 1.25^\circ$ and 32 vertical pressure levels, and the CLM5 shares the same horizontal resolution.

We performed a control run (CTL) and two sets of soil moisture sensitivity experiments. In the CTL experiment, the F2000climo scheme was adopted, in which the Atmosphere and Land model is active, with prescribed sea surface temperatures and sea ice extents derived from merged Reynolds/HADISST products from 1995 to 2005⁶⁰. Other external forcings were set to the climatological monthly mean values. The CTL experiment was integrated for 30 years, and the last 20 years were utilized for the analysis. In this configuration, soil moisture was treated as a prognostic variable. In the climatological soil moisture forced experiment (clm_sm), the global climatological monthly mean soil moisture was used as the forcing field, with the other settings maintaining consistency with those of the CTL experiment. Furthermore, the TP reduced soil moisture experiment (TP_sm) replicated the clm_sm experiment, except that soil moisture values, including all layers over the TP region ($28^\circ\text{--}38^\circ\text{N}$, $80^\circ\text{--}103^\circ\text{E}$) during May–September, were multiplied by 0.5⁶¹. Every case in the soil moisture experiments began running using the initial fields on April 1 of the last 20 years of the CTL experiment and continued until August 31. Differences in the ensemble mean of 20 cases between the TP_sm and clm_sm experiments were analyzed as climate effects of reduced soil moisture over the TP. The significance of the differences was evaluated using a t-test method.

Data availability

All datasets utilized in this study are publicly accessible from the following websites: ECMWF Reanalysis V5 dataset: <https://cds.climate.copernicus.eu/cdsapp#!/search?type=dataset>; Climate Prediction Center in National Oceanic and Atmospheric Administration: <https://psl.noaa.gov/data/gridded/data.cpc.globaltemp.html>; Global Land Data Assimilation System Noah Land Surface Model L4 Version 2.1: https://disc.gsfc.nasa.gov/datasets/GLDAS_NOAH025_M_2.1/summary?keywords=GLDAS. Dataset from China Meteorological Administration Land Data Assimilation System (CLDAS): https://data.cma.cn/data/cdcdetail/dataCode/NAFP_CLDAS2.0_RT.html.

Code availability

The data were analyzed using Python and the NCAR Command Language. All relevant codes used in this study are available upon request from the corresponding author.

Received: 20 August 2024; Accepted: 5 November 2024;

Published online: 17 November 2024

References

- Rogers, C. D. W., Kornhuber, K., Perkins-Kirkpatrick, S. E., Loikith, P. C. & Singh, D. Sixfold increase in historical Northern hemisphere

- concurrent large heatwaves driven by warming and changing atmospheric circulations. *J. Clim.* **35**, 1063–1078 (2022).
- Vogel, M. M., Zscheischler, J., Wartenburger, R., Dee, D. & Seneviratne, S. I. Concurrent 2018 hot extremes across Northern Hemisphere due to human-induced climate change. *Earths Future* **7**, 692–703 (2019).
- Zhou, S., Yu, B. & Zhang, Y. Global concurrent climate extremes exacerbated by anthropogenic climate change. *Sci. Adv.* **9**, eabo1638 (2023).
- Zscheischler, J. et al. A typology of compound weather and climate events. *Nat. Rev. Earth Environ.* **1**, 333–347 (2020).
- Wang, Z., Luo, H. & Yang, S. Different mechanisms for the extremely hot central-eastern China in July–August 2022 from a Eurasian large-scale circulation perspective. *Environ. Res. Lett.* **18** (2023).
- Witze, A. Extreme heatwaves: surprising lessons from the record warmth. *Nature* **608**, 464–465 (2022).
- Jiang, J., Liu, Y., Mao, J. & Wu, G. Extreme heatwave over Eastern China in summer 2022: the role of three oceans and local soil moisture feedback. *Environ. Res. Lett.* **18** (2023).
- Zhang, J., Chen, H., Fang, X., Yin, Z. & Hu, R. Warming-induced hydrothermal anomaly over the Earth's three Poles amplifies concurrent extremes in 2022. *npj Clim. Atmos. Sci.* **7**, 8 (2024).
- Kosaka, Y., Chowdary, J. S., Xie, S.-P., Min, Y.-M. & Lee, J.-Y. Limitations of seasonal predictability for summer climate over East Asia and the Northwestern Pacific. *J. Clim.* **25**, 7574–7589 (2012).
- Di Capua, G. et al. Drivers behind the summer 2010 wave train leading to Russian heatwave and Pakistan flooding. *npj Clim. Atmos. Sci.* **4** (2021).
- Fan, J. et al. Statistical physics approaches to the complex Earth system. *Phys. Rep.* **896**, 1–84 (2021).
- Boers, N. et al. Complex networks reveal global pattern of extreme-rainfall teleconnections. *Nature* **566**, 373–377 (2019).
- Donges, J. F. et al. Unified functional network and nonlinear time series analysis for complex systems science: The pyunicorn package. *Chaos* **25**, 113101 (2015).
- Boers, N., Bookhagen, B., Marwan, N., Kurths, J. & Marengo, J. Complex networks identify spatial patterns of extreme rainfall events of the South American Monsoon System. *Geophys. Res. Lett.* **40**, 4386–4392 (2013).
- Boers, N. et al. Prediction of extreme floods in the eastern Central Andes based on a complex networks approach. *Nat. Commun.* **5**, 5199 (2014).
- Boers, N. et al. The South American rainfall dipole: A complex network analysis of extreme events. *Geophys. Res. Lett.* **41**, 7397–7405 (2014).
- Qiao, P. et al. Extreme rainfall synchronization network between Southwest China and Asia–Pacific region. *Clim. Dyn.* **57**, 3207–3221 (2021).
- Mondal, S. & Mishra, A. K. Complex Networks Reveal Heatwave Patterns and Propagations Over the USA. *Geophys. Res. Lett.* **48**, 12 (2021).
- Wu, Z., Zhang, P., Chen, H. & Li, Y. Can the Tibetan Plateau snow cover influence the interannual variations of Eurasian heat wave frequency? *Clim. Dyn.* **46**, 3405–3417 (2015).
- Deng, K., Yang, S., Ting, M., Lin, A. & Wang, Z. An Intensified Mode of Variability Modulating the Summer Heat Waves in Eastern Europe and Northern China. *Geophys. Res. Lett.* **45** (2018).
- Petoukhov, V., Rahmstorf, S., Petri, S. & Schellnhuber, H. J. Quasiresonant amplification of planetary waves and recent Northern Hemisphere weather extremes. *Proc. Natl Acad. Sci. Usa.* **110**, 5336–5341 (2013).
- Coumou, D., Petoukhov, V., Rahmstorf, S., Petri, S. & Schellnhuber, H. J. Quasi-resonant circulation regimes and hemispheric synchronization of extreme weather in boreal summer. *Proc. Natl Acad. Sci. Usa.* **111**, 12331–12336 (2014).

23. Kornhuber, K. et al. Amplified Rossby waves enhance risk of concurrent heatwaves in major breadbasket regions. *Nat. Clim. Change* **10**, 48–53 (2019).
24. Lin, Q. & Yuan, J. Linkages between Amplified Quasi-stationary Waves and Humid Heat Extremes in Northern Hemisphere Midlatitudes. *J. Clim.* **35**, 8245–8258 (2022).
25. Liu, Y. M. et al. Land-atmosphere-ocean coupling associated with the Tibetan Plateau and its climate impacts. *Natl Sci. Rev.* **7**, 534–552 (2020).
26. Huang, J. et al. Global Climate Impacts of Land-Surface and Atmospheric Processes Over the Tibetan Plateau. *Rev. Geophys.* **61** (2023).
27. Xie, Y. et al. Oceanic repeaters boost the global climatic impact of the Tibetan Plateau. *Sci. Bull.* **68**, 2225–2235 (2023).
28. Yao, T., Thompson, L., Chen, D. & Piao, S. Reflections and future strategies for Third Pole Environment. *Nat. Rev. Earth Environ.* **3**, 608–610 (2022).
29. Ma, T., Wu, G., Liu, Y. & Mao, J. Abnormal warm sea-surface temperature in the Indian Ocean, active potential vorticity over the Tibetan Plateau, and severe flooding along the Yangtze River in summer 2020. *Q. J. R. Meteorol. Soc.* **148**, 1001–1019 (2022).
30. Jiang, J. et al. Southeast China Extreme Drought Event in August 2019: Context of Coupling of Midlatitude and Tropical Systems. *J. Clim.* **35**, 3699–3713 (2022).
31. Lu, M., Huang, B., Li, Z., Yang, S. & Wang, Z. Role of Atlantic air–sea interaction in modulating the effect of Tibetan Plateau heating on the upstream climate over Afro-Eurasia–Atlantic regions. *Clim. Dyn.* **53**, 509–519 (2018).
32. Lu, M. et al. Possible effect of the Tibetan Plateau on the “upstream” climate over West Asia, North Africa, South Europe and the North Atlantic. *Clim. Dyn.* **51**, 1485–1498 (2017).
33. Nan, S., Zhao, P. & Chen, J. Variability of summertime Tibetan tropospheric temperature and associated precipitation anomalies over the central-eastern Sahel. *Clim. Dyn.* **52**, 1819–1835 (2018).
34. Zhang, P. F., Liu, Y. M. & He, B. A. Impact of East Asian Summer Monsoon Heating on the Interannual Variation of the South Asian High. *J. Clim.* **29**, 159–173 (2016).
35. Dong, W., Jia, X. & Wu, R. Impact of summer Tibetan Plateau snow cover on the variability of concurrent compound heatwaves in the Northern Hemisphere. *Environ. Res. Lett.* **19** (2023).
36. Seneviratne, S. I. et al. Investigating soil moisture–climate interactions in a changing climate: A review. *Earth-Sci. Rev.* **99**, 125–161 (2010).
37. Martius, O., Wehrli, K. & Rohrer, M. Local and remote atmospheric responses to soil moisture anomalies in Australia. *J. Clim.* **34**, 9115–9131 (2021).
38. Yoon, D. et al. Role of land–atmosphere interaction in the 2016 Northeast Asia heat wave: Impact of soil moisture initialization. *J. Geophys. Res.: Atmospheres* **128**, e2022JD037718 (2023).
39. Fan, K. et al. Spatiotemporal impact of soil moisture on air temperature across the Tibet Plateau. *Sci. Total Environ.* **649**, 1338–1348 (2019).
40. Liu, Y. M., Wu, G. X., Liu, H. & Liu, P. Condensation heating of the Asian summer monsoon and the subtropical anticyclone in the Eastern Hemisphere. *Clim. Dyn.* **17**, 327–338 (2001).
41. Enomoto, T., Hoskins, B. J. & Matsuda, Y. The formation mechanism of the Bonin high in August. *Q. J. R. Meteorol. Soc.* **129**, 157–178 (2003).
42. White, R. H., Kornhuber, K., Martius, O. & Wirth, V. From Atmospheric Waves to Heatwaves: A Waveguide Perspective for Understanding and Predicting Concurrent, Persistent, and Extreme Extratropical Weather. *Bull. Am. Meteorol. Soc.* **103**, E923–E935 (2022).
43. Li, Q. et al. A zonally-oriented teleconnection pattern induced by heating of the western Tibetan Plateau in boreal summer. *Clim. Dyn.* **57**, 2823–2842 (2021).
44. Hoskins, B. J. & Ambrizzi, T. Rossby-wave propagation on a realistic longitudinally varying flow. *J. Atmos. Sci.* **50**, 1661–1671 (1993).
45. Lu, R., Oh, J. & Kim, B. A teleconnection pattern in upperlevel meridional wind over the North African and Eurasian continent in summer. *Tellus A: Dyn. Meteorol. Oceanogr.* **54**, 44–55 (2002).
46. Takaya, K. & Nakamura, H. A formulation of a phase-independent wave-activity flux for stationary and migratory quasigeostrophic eddies on a zonally varying basic flow. *J. Atmos. Sci.* **58**, 608–627 (2001).
47. Sun, J. Record-breaking SST over mid-North Atlantic and extreme high temperature over the Jianghuai–Jiangnan region of China in 2013. *Chin. Sci. Bull.* **59**, 3465–3470 (2014).
48. He, C., Zhou, T., Zhang, L., Chen, X. & Zhang, W. Extremely hot East Asia and flooding western South Asia in the summer of 2022 tied to reversed flow over Tibetan Plateau. *Clim. Dyn.* **61**, 2103–2119 (2023).
49. Seneviratne, S. I., Fischer, E. M., Vidale, P. L., Lüthi, D. & Schär, C. Soil Moisture–Atmosphere Interactions during the 2003 European Summer Heat Wave. *J. Clim.* **20**, 5081–5099 (2007).
50. Fan, Y. & van den Dool, H. Climate Prediction Center global monthly soil moisture data set at 0.5° resolution for 1948 to present. *J. Geophys. Res.: Atmosph.* **109** (2004).
51. Rodell, M. et al. The Global Land Data Assimilation System. *Bull. Am. Meteor. Soc.* **85**, 381–394 (2004).
52. Liu, J., Shi, C., Sun, S., Liang, J. & Yang, Z.-L. Improving Land Surface Hydrological Simulations in China Using CLDAS Meteorological Forcing Data. *J. Meteorol. Res.* **33**, 1194–1206 (2020).
53. Hersbach, H. et al. The ERA5 global reanalysis. *Q. J. R. Meteorol. Soc.* **146** (2020).
54. Muñoz-Sabater, J. et al. ERA5-Land: a state-of-the-art global reanalysis dataset for land applications. *Earth Syst. Sci. Data* **13**, 4349–4383 (2021).
55. Grotjahn, R. & Faure, G. Composite Predictor Maps of Extraordinary Weather Events in the Sacramento, California, Region. *Wea. Forecasting* **23**, 313–335 (2008).
56. Wu, X. & Mao, J. Interdecadal modulation of ENSO-related spring rainfall over South China by the Pacific Decadal Oscillation. *Clim. Dyn.* **47**, 3203–3220 (2016).
57. Watanabe, M. & Kimoto, M. Atmosphere–ocean thermal coupling in the North Atlantic: A positive feedback. *Q. J. R. Meteorol. Soc.* **126**, 3343–3369 (2000).
58. Watanabe, M. & Jin, F. F. A moist linear baroclinic model: coupled dynamical–convective response to El Niño. *J. Clim.* **16**, 1121–1139 (2003).
59. Danabasoglu, G. et al. The Community Earth System Model Version 2 (CESM2). *J. Adv. Model. Earth Syst.* **12** (2020).
60. Rosinski, J., Caron, J. M., Shea, D., Hack, J. J. & Hurrell, J. W. A New Sea Surface Temperature and Sea Ice Boundary Dataset for the community atmosphere model. *J. Clim.* **21**, 5145–5153 (2008).
61. Zhou, J., Zuo, Z. Y. & Rong, X. Y. Comparison of the effects of soil moisture and El Niño on summer precipitation in eastern China. *Sci. China-Earth Sci.* **63**, 267–278 (2020).

Acknowledgements

This work was supported by the National Natural Science Foundation of China (42288101), the China Postdoctoral Science Foundation (2023M733453), and the National Key Scientific and Technological Infrastructure project “Earth System Science Numerical Simulator Facility” (EarthLab). J.F. was supported by the National Natural Science Foundation of China (12275020, 12135003, 12205025), the National Key Research and Development Program of China (2023YFE0109000), and the Fundamental Research Funds for the Central Universities.

Author contributions

Y.L. and J.J. conceived and designed the study; J.J., Y.L., J.M., B.H., and J.F. performed the numerical experiments and data analysis; J.J., Y.L., and

J.M. drafted the manuscript; G.W., J.F., B.H., T.M., and W.B. provided comments and helped improve the manuscript. All the authors discussed the results and contributed to the writing of the manuscript.

Competing interests

The authors declare no competing interests.

Additional information

Supplementary information The online version contains supplementary material available at

<https://doi.org/10.1038/s41612-024-00831-x>.

Correspondence and requests for materials should be addressed to Yimin Liu or Jingfang Fan.

Reprints and permissions information is available at

<http://www.nature.com/reprints>

Publisher's note Springer Nature remains neutral with regard to jurisdictional claims in published maps and institutional affiliations.

Open Access This article is licensed under a Creative Commons Attribution-NonCommercial-NoDerivatives 4.0 International License, which permits any non-commercial use, sharing, distribution and reproduction in any medium or format, as long as you give appropriate credit to the original author(s) and the source, provide a link to the Creative Commons licence, and indicate if you modified the licensed material. You do not have permission under this licence to share adapted material derived from this article or parts of it. The images or other third party material in this article are included in the article's Creative Commons licence, unless indicated otherwise in a credit line to the material. If material is not included in the article's Creative Commons licence and your intended use is not permitted by statutory regulation or exceeds the permitted use, you will need to obtain permission directly from the copyright holder. To view a copy of this licence, visit <http://creativecommons.org/licenses/by-nc-nd/4.0/>.

© The Author(s) 2024